

CLEAN OPTICAL SPECTRUM OF THE RADIO JET OF 3C 120

S. F. SÁNCHEZ,¹ B. GARCIA-LORENZO,² E. MEDIAVILLA,² J. I. GONZÁLEZ-SERRANO,^{3,4} AND L. CHRISTENSEN¹

Received 2004 June 11; accepted 2004 July 8

ABSTRACT

We present integral field spectroscopy (IFS) of the central region of 3C 120. We have modeled the nuclear and host galaxy three-dimensional spectra using techniques normally applied to imaging, decoupling both components and obtaining a residual data cube. Using this residual data cube, we detected the extended emission line region associated with the radio jet. We obtained, for the first time, a clean spectrum of this region and found compelling evidence of a jet-cloud interaction. The jet compresses and splits the gas cloud, which is ionized by the active galactic nucleus (AGN) and/or by the strong local UV photon field generated by a shock process. We cannot confirm the detection of an extended emission line region associated with the counterjet reported by Axon and coworkers.

Subject headings: galaxies: active — galaxies: individual (3C 120) — galaxies: ISM — galaxies: jets

Online material: color figures

1. INTRODUCTION

3C 120 is a Seyfert 1 radio galaxy at a redshift of 0.033 with a compact flat-spectrum radio core and a powerful X-ray emission (Halpern 1985). It has a one-sided superluminal radio jet with two clear knots at 4'' west and 25'' northwest from the core (Walker et al. 1987, 1988; Walker 1997). Morphologically it is a bulge-dominated galaxy with several continuum and extended emission line regions (EELR; Baldwin et al. 1980; Wlerick et al. 1981; Pérez-Fournon et al. 1986; Hua 1988; Soubeyran et al. 1989), indicating a change of star formation history and a combination of different ionization mechanisms from region to region.

The radio jet shows a continuum-dominated optical counterpart, consistent with synchrotron radiation, that extends from 7'' to 25'' out of the nucleus, but without a clear counterpart at the location of the 4'' knot (Hjorth et al. 1995). X-ray emission associated with the 25'' knot has been detected (Harris et al. 1999). An EELR has been detected at $\sim 1''$ distance from the 4'' knot, the so called E1 region (Soubeyran et al. 1989). This EELR has been detected using different spectroscopic and imaging techniques (e.g., Baldwin et al. 1980; Wlerick et al. 1981; Hua 1988; Soubeyran et al. 1989; Axon et al. 1989). Axon et al. (1989) showed that it comprises two kinematic components, separated by $\sim 150 \text{ km s}^{-1}$, with a south-north gradient.

This EELR does not originate in material that has been ejected with the radio-emitting plasma. It arises because of the interaction, most probably lateral expansion, of the radio jet with the interstellar medium (ISM) of the galaxy (Axon et al. 1989). Very little is known about the ionization conditions or the amount of dust in this area. Hua (1988) estimated roughly an $[\text{O III}] \lambda 5007/\text{H}\beta$ ratio of ~ 17 for this cloud, based on the data from Baldwin et al. (1980), which contrasts with the value found for the nucleus (~ 1). These values were derived without

a proper deblending of the broad and narrow emission lines, and without decontaminating the spectrum of the E1 region from the contribution of the host galaxy.

2. OBSERVATIONS AND DATA REDUCTION

We obtained integral field spectroscopy (IFS) of the core of 3C 120 using INTEGRAL (Arribas et al. 1998) at the William Herschel Telescope (WHT) to derive a clean spectrum of the E1 region. The observations were done on 2003 February 26, under photometric conditions and with an average seeing disk of 1.2 FWHM. We obtained three exposures of 1200 s each, using the SB2 fiber bundle, which comprises 219 fibers (189 science+30 sky fibers), each 0.9 in diameter projected on the sky, covering a total field of view of $\sim 16'' \times 12''$. We used the low-resolution V300 grating centered at $\sim 5500 \text{ \AA}$, with a nominal spectral resolution of ~ 450 at the central wavelength, covering the range 3500–9000 \AA , with a final sampling of $\sim 3 \text{ \AA}$ per pixel. A detailed explanation of the data reduction and calibration will be presented elsewhere (B. Garcia-Lorenzo et al., in preparation). It basically comprises the standard steps, including bias subtraction, spectra extraction, flat-fielding, and wavelength and flux calibration. Finally, an interpolation routine was applied over each monochromatic slice using E3D (Sánchez 2004) to obtain a regular grid data cube with 0.3 arcsec² pixels. For comparison purposes we obtained a WFC F555W-band image of 3C 120, available from the archive of the *Hubble Space Telescope (HST)*. This image has a 3σ limiting surface brightness magnitude of $\sim 25.5 \text{ mag arcsec}^{-2}$, deep enough for the purposes of this article. Because of the width of the F555W band, this image traces the morphology of the continuum emission in 3C 120.

3. ANALYSIS AND RESULTS

We create a model from the F555W-band image of the object using an isophotal surface brightness analysis, following the prescriptions described by Jedrzejewski (1987). The model was subtracted from the original image, producing a residual image. Hjorth et al. (1995) and Soubeyran et al. (1989) used this technique to detect the optical counterpart of the radio jet in 3C 120 and the EELRs, respectively. Figure 1 shows the resulting residual image in an arbitrary gray scale, together

¹ Astrophysikalisches Institut Potsdam, An der Sternwarte 16, 14482 Potsdam, Germany; ssanchez@aip.de.

² Instituto de Astrofísica de Canarias, 38205 La Laguna, Tenerife, Spain.

³ Instituto de Física de Cantabria, UC-CSIC, Avenida de Los Castros S/N, 35005 Santander, Spain.

⁴ Departamento de Física Moderna, Facultad de Ciencias, UC, Avenida de Los Castros S/N, 35005 Santander, Spain.

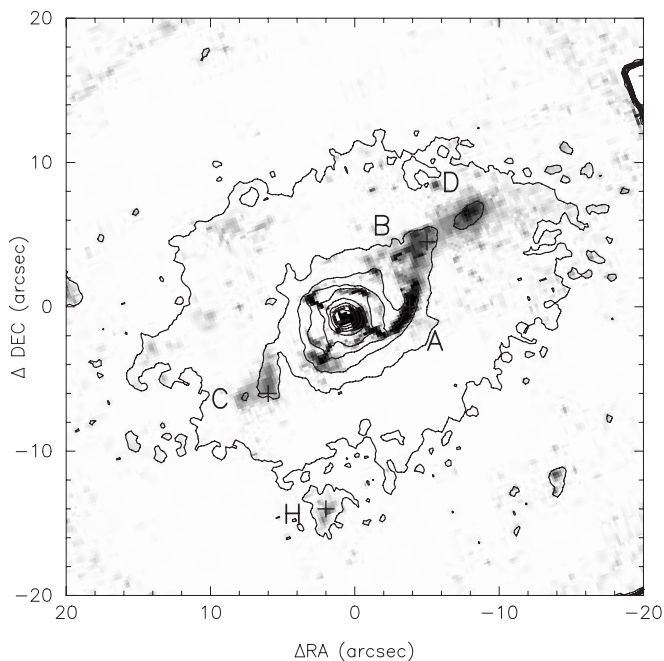


FIG. 1.—Contour plot of the F555W-band image of 3C 120 obtained with the *HST* WFPC2. The gray scale shows the residuals after subtracting the smooth component by an isophotal analysis. The spikes of the WFC PSF are clearly seeing. We have marked the position of the continuum-dominated substructures using the nomenclature of Soubeyran et al. (1989). [See the electronic edition of the *Journal* for a color version of this figure.]

with the contours of the original image. The different continuum-dominated substructures detected by Soubeyran et al. (1989) are indicated in the figure using their nomenclature. As expected, there is no trace of the emission-line-dominated substructures.

The top left panel of Figure 2 shows the intensity map of the [O III] $\lambda 5007$ emission line (*contours*) and the adjacent continuum (*gray scale*). These maps have been created coadding the intensities of the 5170–5200 Å and 5204–5246 Å wavelength ranges in the data cube, respectively, and subtracting the continuum from the emission line map. The emission line map is remarkably similar to the narrowband image presented by Hua (1988), showing a strong gaseous emission extended through out the host galaxy. Despite the strong contamination from the nucleus and the host galaxy, it is possible to identify the [O III] EELRs described by Soubeyran et al. (1989) (marked as E1, E2, and E3). To derive clean spectra of these substructures, we create a galaxy+nucleus three-dimensional template data cube and subtract it from the data.

First, we create for each wavelength a narrowband image of the width of one spectral pixel (~ 3 Å) from the original data cube. Then we model the object at each of these *monochromatic* images using two different techniques widely used the analysis of two-dimensional images: (1) a two-dimensional image modeling of the nucleus and the host and (2) an isophotal modeling based on a surface brightness analysis. The first method has the advantage that it also provides us with a decoupled spectra of the nucleus and the host galaxy (see Jahnke et al. 2004). Previous attempts to do so have used longslit spectroscopy, with the inherent limitations due to the loss of the two-dimensional information (Jahnke 2002). A similar technique has been used successfully for the deblending of QSO lenses with IFS (Wisotzki et al. 2003). However, this method has the disadvantage that it requires a good estimation

of the PSF, and it requires more assumptions about the morphology of the object (i.e., more parameters to fit). A more detailed description of the technique and its limitations will be presented elsewhere (S. F. Sánchez et al., in preparation).

The two-dimensional image modeling of the nucleus and the host for each *monochromatic* image is performed using GALFIT (Peng et al. 2002). This program has been extensively tested in the image decomposition of QSOs and their hosts (Sánchez et al. 2004). The two-dimensional model comprises a narrow Gaussian function (to model the nucleus) and a de Vaucouleurs law (to model the galaxy), both convolved with a PSF. The PSF was obtained from a calibration star data cube, observed just before the object. The structural parameters of the host galaxy (P.A., ellipticity, and effective radius) were obtained by a two-dimensional modeling of the F555W-band image. The fit over the data cube was performed twice: (1) leaving the centroid of the object and the intensities of both components free, and (2) fixing the centroid by the result of a polynomial fitting as a function of the wavelength over the results of the first fit. This increases the accuracy of the recovered spectra (see Wisotzki et al. 2003). The final three-dimensional data cube model is then subtracted from the original data cube to get a residual data cube.

As a second method, we perform a surface brightness analysis of each monochromatic image, using the same code that we used for the analysis of the F555W-band image (Fig. 1). This method provides us with a two-dimensional model of the object, which we subtract from the original image to obtain a residual image for each wavelength. As in the previous method, the technique was applied twice: (1) once to let the program look for the best elliptical isophote at each radii (the centroid, P.A., ellipticity, and intensity are free parameters); and (2) once more to fix all the parameters but the intensity to the values derived from a polynomial fitting as a function of the wavelength over the results of the first pass. We subtract the final three-dimensional model from the original data to obtain a residual data cube.

The residual data cubes obtained using the two techniques are quite similar. However, the residual produced by the first method shows a ring structure in the inner region at any wavelength. This structure, ~ 1000 times fainter than the peak intensity of the nucleus, is not seen in the residual of the F555W-band image. Similar structures are normally found in this kind of two-dimensional modeling because of inaccuracies in the determination of the PSF. This was true in our case, since we have clearly undersampled the PSF. Although it does not strongly affect the extracted spectra of the nucleus and the host, it introduces a non-Poissonian noise in the residual data cube. Because of that, we restricted our analysis of the residuals to the data cube obtained with the second method, using the first method only for deblending the host and nucleus contributions.

It is important to note here that the PSF undersampling does not affect the accuracy of the centroid determination, fundamental to compare images taken with different instruments. The displacement of the object along the field of view at different wavelengths due to differential atmospheric refraction (Filippenko 1982) can be used to determine the centroid position with high precision (Mediavilla et al. 1998; Arribas et al. 1999; Wisotzki et al. 2003). The accuracy in the determination of the centroid in our IFS was better than $0''.1$, at any wavelength (S. F. Sánchez et al., in preparation).

The top right panel of Figure 2 shows a contour plot of the narrowband image at the continuum adjacent to the [O III] $\lambda 5007$ emission lines (5204–5246 Å) extracted from the

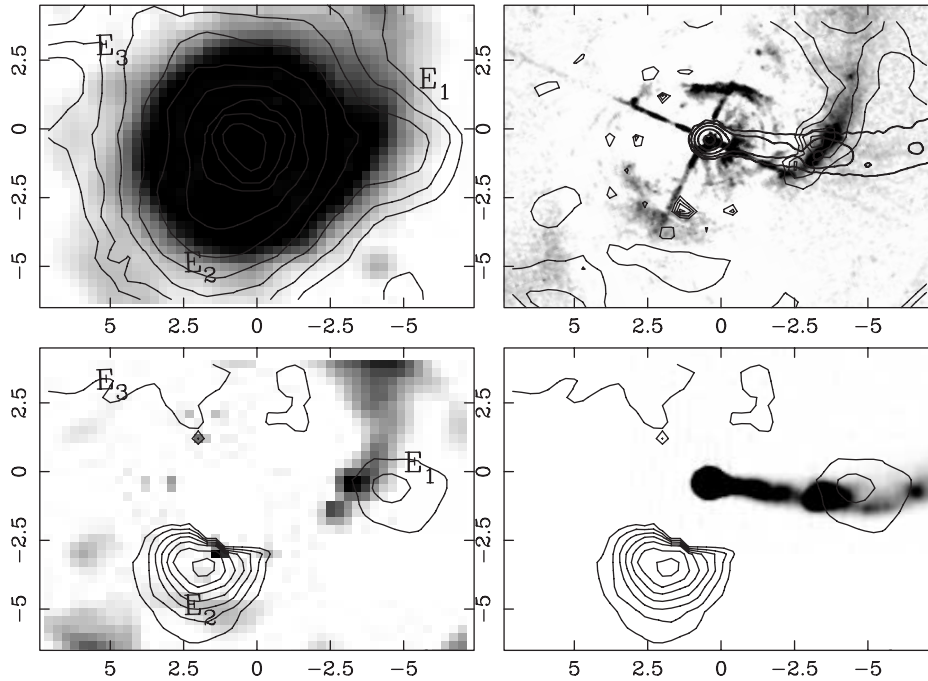


FIG. 2.—*Top left*: Contour plot of a narrowband image centred on the $[\text{O III}]\lambda 5007$ emission line at the redshift of the object (5170–5200 Å) together with a gray-scale narrowband image of the adjacent continuum (5204–5246 Å) obtained from the original data cube. The continuum emission was subtracted from the emission-line map. The contours start at $0.5 \times 10^{-16} \text{ ergs s}^{-1} \text{ cm}^{-2} \text{ \AA}^{-1}$, with 0.25 dex separation between each one. E1, E2, and E3 indicate the $[\text{O III}]\lambda 5007$ emission areas with the nomenclature of Soubeyran et al. (1989). *Top right*: Contour plot of a narrowband image centered on the continuum adjacent to the $[\text{O III}]\lambda 5007$ emission line (5204–5246 Å) obtained from the residual data cube, together with a gray-scale of the residual from the *HST* F555W broadband image (Fig. 1). The contours start at $0.02 \times 10^{-16} \text{ ergs s}^{-1} \text{ cm}^{-2} \text{ \AA}^{-1}$, with a separation of $0.015 \times 10^{-16} \text{ ergs s}^{-1} \text{ cm}^{-2} \text{ \AA}^{-1}$. The blue contours extending to the right show the map of the radio jet at 4885 MHz. *Bottom left*: Contour plot of a narrowband image centered on the $[\text{O III}]\lambda 5007$ emission line (5170–5200 Å) together with a gray scale of the adjacent continuum (5204–5246 Å) obtained from the residual data cube. The contours start at $0.5 \times 10^{-16} \text{ ergs s}^{-1} \text{ cm}^{-2} \text{ \AA}^{-1}$, with a separation of $0.3 \times 10^{-16} \text{ ergs s}^{-1} \text{ cm}^{-2} \text{ \AA}^{-1}$. *Bottom right*: The same contour plot as in the bottom left panel, together with a gray scale of the map of the radio jet at 4885 MHz. We cannot confirm the detection of an EELR associated with the undetected counterjet, reported by Axon et al. (1989), at $\sim 5''$ east from the nucleus. [See the electronic edition of the *Journal* for a color version of this figure.]

residual data cube. The gray scale shows the residual of the continuum-dominated F555W-band image. Both images were recentered by matching the peak of the central pointlike source in the F555W-band image with the centroid of the object in the IFS data. The accuracy of the determination of the position of the peak in the *HST* image is a fraction of the pixel. Thus, the error in the recentering was dominated by the error in the determination of the centroid in the IFS data ($< 0''.1$, as quoted above). We used the rotator angle of the WHT and the WCS of the *HST* image to align both images in the sky. Despite the superior resolution of the *HST* image, the agreement between the two maps is remarkable. There is an expected mismatch in the inner regions, where the arc structures seen in the *HST* image are not detected in the IFS map. This is a combined effect of the wider PSF and the worse sampling, which reduces the structural information in the inner regions. However, the A, B, and C continuum-dominated substructures (see Fig. 1) are clearly identified in the IFS residual map. This comparison demonstrates that the applied technique is valid for recovering the substructures in this object. We overplotted the radio map at 4885 MHz, using its WCS to align them with the *HST* and IFS data. The radio data were taken using the VLA in the A configuration, with a beam of $0''.35 \times 0''.35$ Walker (1997). There is no evident connection between the continuum structures and the radio jet. We will discuss elsewhere the nature of these structures (B. García-Lorenzo, in preparation).

The bottom left panel of Figure 2 shows the contour plot of the narrowband image centered at the emission line $[\text{O III}]\lambda 5007$, at the redshift of the object (5170–5200 Å), extracted

from the residual data cube. The gray scale shows the same narrowband image of the continuum adjacent to this line as shown in the top right panel. The EELRs are now clearly distinguished. There is no clear correspondence between the continuum-dominated substructures and these emission-line-dominated ones. The bottom right panel shows the same contour plot together with a gray-scale representation of the radio map. The center of the E1 region is located at $\sim 1''$ northwest of the radio knot at $4''$ (Soubeyran et al. 1989), just coincident with the bend in the radio jet, which passes across the EELR. Despite of the projection effects, this indicates most probably a physical connection between them (Axon et al. 1989; Soubeyran et al. 1989). We cannot confirm the detection reported by Axon et al. (1989) of an EELR associated with the undetected counterjet at $\sim 5''$ east from the nucleus.

The top panel of Figure 3 shows the integrated spectrum of 3C 120 in the wavelength range between 3700 and 7300 Å, together with the nucleus and host spectra obtained from the two-dimensional fitting technique. The detected emission lines are indicated with their corresponding names. A detail of the spectra in the $[\text{O III}]\lambda 5007/\text{H}\beta$ spectral region is also presented. The spectrum of the nucleus is clearly bluer than that of the host galaxy. It contains all the broad emission lines, as expected. The narrow emission lines are considerably fainter than the broad emission lines. We only detected the $[\text{O III}]\lambda 5007$ and $[\text{N II}]\lambda 6583$ lines (that blended with the broad $\text{H}\alpha$). The average host galaxy spectrum contains almost all the narrow emission lines. Recent results indicate that the ionized gas producing the observed narrow emission line in active galactic nuclei (AGNs) can extend

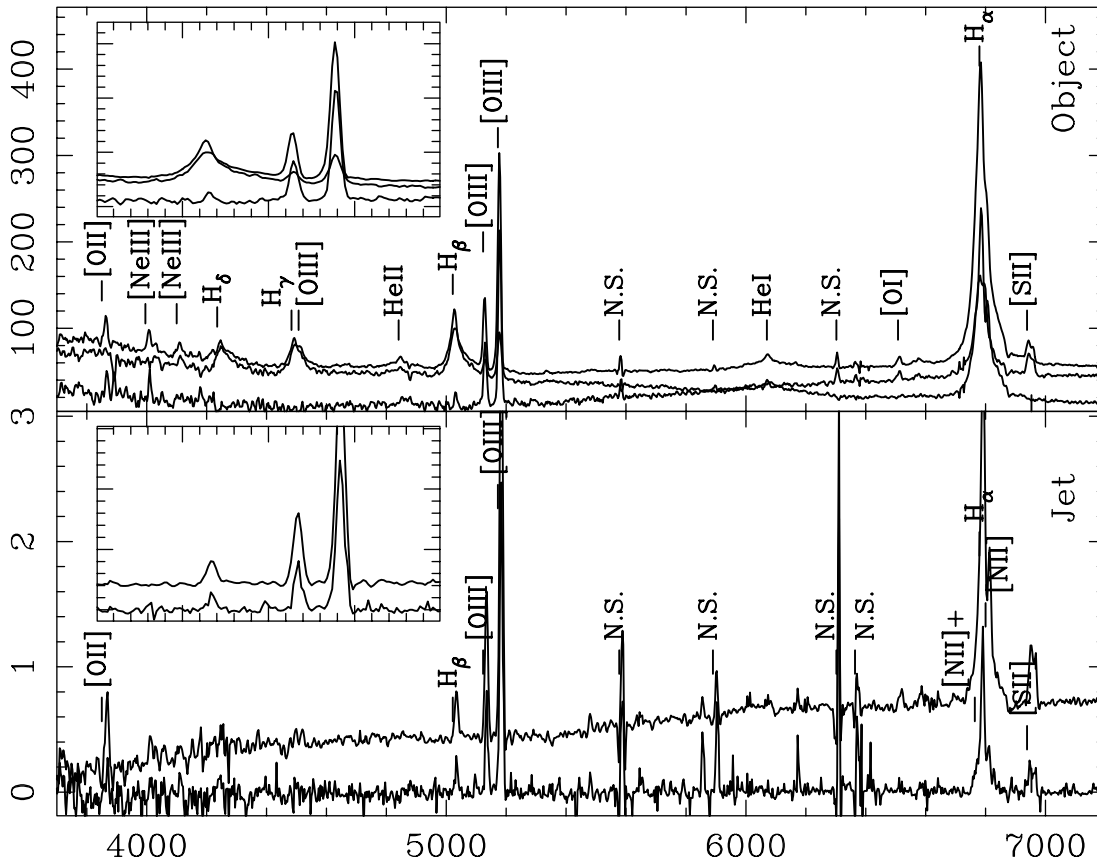


FIG. 3.—*Top*: Integrated spectrum of 3C 120 over the field of view of our observations in the wavelength range 3700–7200 Å, in units of 10^{-16} ergs s^{-1} cm^{-2} \AA^{-1} , with a detail over the [O III]– $H\beta$ spectral range (*small box*). The two bottom lines show the integrated spectrum of the nucleus and host galaxy, respectively, obtained from the two-dimensional fitting. *Bottom*: Integrated spectrum of the E1 area of the residual data cube after model subtraction in similar wavelength ranges. We have included the spectrum of the same area before the subtraction of the smooth component as the upper line. In both panels we have marked the detected emission lines. [See the electronic edition of the *Journal* for a color version of this figure.]

throughout all the host galaxy (Jahnke 2002; Jahnke et al. 2004). There is no clear 4000 Å break in the host spectrum, but a rise up in the blue–UV spectral range. This indicates most probably a large amount of star formation and/or a very young stellar population (Baldwin et al. 1980; Moles et al. 1988). However, the line ratios, $\log_{10}([\text{O III}] \lambda 5007/H\beta) = 1.63$ and $\log_{10}([\text{N II}]/H\alpha) = -0.39$, indicate that the dominant ionization source of the gas in this galaxy is the AGN. The average dust content is high, with a Balmer ratio of $H\alpha/H\beta \sim 10$ ($A_V \sim 4$ mag). We cannot confirm the [O III] $\lambda 5007/H\beta$ values near to ~ 1 in the nuclear regions, reported by Baldwin et al. (1980) and Hua (1988). Taking an average spectrum of the nucleus ($1''$ aperture radius), once decontaminated from the broad emission line by a line-fitting deblending, we find a ratio remarkably similar to the average over the whole galaxy: $\log_{10}([\text{O III}] \lambda 5007/H\beta) = 1.04$.

The bottom panel of Figure 3 shows the *clean* spectrum of the E1 region, obtained by co-adding the spectra of the residual data cube in a $1''$ aperture centered in that region. For comparison, we plotted the spectrum of this area before decontamination (i.e., a nonclean spectrum). The differences between the spectra are clearly identified. The clean spectrum is an emission-line-dominated spectrum, as expected from pure ionized gas, with no significant continuum. On the other hand, the nonclean spectrum has a significant continuum contribution, and its emission lines are ~ 2.4 times brighter, which indicates a strong contamination from the host galaxy. The Balmer ratio is $H\alpha/H\beta \sim 4$ ($A_V \sim 1$ mag) for the nonclean

spectrum, in contrast to the $H\alpha/H\beta \sim 7$ ($A_V \sim 3$ mag) value for the clean one. The [O III] $\lambda 5007/H\beta$ and [N II]/ $H\alpha$ line ratios, ~ 1.4 and ~ -0.4 , are similar in the clean and nonclean spectra. They are also similar to the ratios found in the average host galaxy spectrum.

Based on the above quoted line ratios, the main mechanisms which might be involved in the emission line processes are: (1) photoionization by a hard UV continuum, emitted most probably by the AGN, and (2) high-velocity radiative shocks, which can influence the emission line processes through the generation of a strong local UV photon field in the host post-shock zone. Both processes can generate the observed line ratios, under certain physical conditions (Veilleux & Osterbrock 1987; Dopita & Sutherland 1995). On the other hand, the line ratios exclude photoionization from a star-forming region (Veilleux & Osterbrock 1987).

In the case of photoionization by the AGN, there is a simple relation between the $H\beta$ and the nearby continuum luminosity (e.g., 4861 Å), assuming a power law for the ionizing continuum (Osterbrock 1989). Using the dust-corrected $H\beta$ luminosity, the ionizing continuum should have an intensity of $\sim 0.4 \times 10^{-16}$ ergs s^{-1} cm^{-2} \AA^{-1} at 4861 Å. This intensity can be compared with the flux received by the E1 region from the AGN, using the spectrum of the nucleus described above. Assuming an isotropic emission and a $\sim 1/r^2$ decay of the flux, and considering that the E1 region has a diameter of ~ 2 kpc (Axon et al. 1989) and is at a distance of ~ 10 kpc from the nucleus, this flux is $\sim 0.3 \times 10^{-16}$ ergs s^{-1} cm^{-2} \AA^{-1} . Under

these assumptions, the amount of UV flux received by the E1 region from the AGN would be enough to photoionize it.

Assuming a photoionization mechanism, we can derive the physical conditions in the cloud (Osterbrock 1989). Using the upper limit to the flux of the undetected [O III] $\lambda 4364$ line and the relation between the temperature and the ([O III] $\lambda 5007 + 4959$)/[O III] $\lambda 4363$ flux ratio, we obtain an upper limit to the effective temperature in the E1 region of 55,000 K. We estimated the electron density, $n_e \sim 160 \text{ cm}^{-3}$, using the line ratio [S II] $\lambda 6716/\lambda 6731$ (~ 1.3 for the clean spectrum) and the relation between this ratio and the density (assuming a temperature of $\sim 10^4$ K). These values are similar to those found in the EELRs associated with jet-cloud interactions in other radio galaxies (e.g., Villar-Martín et al. 1999; Solórzano-Iñarrea & Tadhunter 2003).

A postshock zone can also give rise to the observed line ratios in the case of high shock velocities, $\sim 350\text{--}500 \text{ km s}^{-1}$, and low magnetic fields, $B/(\mu G) \sim 0 \text{ cm}^{3/2}$ (Dopita & Sutherland 1995). These velocities are in the range of the lateral expansion velocity estimated by Axon et al. (1989) for E1, $\sim 350\text{--}700 \text{ km s}^{-1}$, assuming a projection angle $\sim 12^\circ\text{--}24^\circ$. However, such a low magnetic field implies a density lower than the previously derived from the [S II] line ratio. Dopita & Sutherland (1995) already noticed that under the effects of a shock, the density derived from the [S II] line ratio is unreliable, because of the compression and the change of ionization stage in different regions. For low magnetic fields this ratio can be ~ 1.3 for a preshock density of 1 cm^{-3} . Dopita & Sutherland (1996) determined the relation between the $H\beta$ luminosity in the postshock zone and the shock velocity and electron density. Using this relation, a shock velocity of $\sim 340 \text{ km s}^{-1}$ is required to reproduce the observed luminosity of $H\beta$. This velocity is similar to the estimated lateral expansion speed quoted above. Therefore, a shock process could also ionize the E1 region.

4. CONCLUSIONS

We developed a new technique for decoupling the spectra of different components in nearby galaxies and AGNs, using IFS. Using it we obtained, for the first time, the decoupled spectra of the nucleus and the host galaxy of 3C 120, and a clean spectrum of the EELR associated with its radio jet. Two different mechanisms could cause the ionization of this region: direct photoionization by the AGN or by UV photons emitted by the gas cooling behind a shock front. In both cases, there is compelling evidence that the jet-cloud interaction plays a major role. (1) The lateral expansion of the jet and its interaction with the ISM is, most probably, the reason for the density enhancement in the E1 area (Axon et al. 1989). (2) In the case of direct photoionization, the UV flux needs to reach the region without substantial absorption. The jet itself, which has associated high-energetic particles, can destroy the dust grains, creating the observed dust decrease in this region. (3) In the case of a shock ionization, the lateral expansion of the jet produces the shock itself. Perhaps the combined effect of a direct AGN and a shock induced photoionization has to be considered in order to understand the ionization of the E1 region.

This project is part of the Euro3D RTN on IFS, funded by the EC under contract HPRN-CT-2002-00305. The WHT is operated on the island of La Palma by the Isaac Newton Group in the Spanish Observatorio del Roque de los Muchachos of the IAC. This project has used images obtained from the *HST* archive, using the ESO archiving facilities. We would like to thank R. C. Walker, who has kindly provided us with the radio maps of 3C 120. We would like to thank the anonymous referee, who has helped us to improve the quality of this paper with his/her remarks.

REFERENCES

- Arribas, S., Mediavilla, E., García-Lorenzo, B., del Burgo, C., & Fuensalida, J. J. 1999, *A&AS*, 136, 189
- Arribas, S., et al. 1998, in *Proc. SPIE*, 3355, 821
- Axon, D. J., Pedlar, A., Unger, S. W., Meurs, E. J. A., & Whittle, D. M. 1989, *Nature*, 341, 631
- Baldwin, J. A., Carswell, R. F., Wampler, E. J., Boksenberg, A., Smith, H. E., & Burbidge, E. M. 1980, *ApJ*, 236, 388
- Dopita, M. A., & Sutherland, R. S. 1995, *ApJ*, 455, 468
- . 1996, *ApJS*, 102, 161
- Filippenko, A. V. 1982, *PASP*, 94, 715
- Halpern, J. P. 1985, *ApJ*, 290, 130
- Harris, D. E., Hjorth, J., Sadun, A. C., Silverman, J. D., & Vestergaard, M. 1999, *ApJ*, 518, 213
- Hjorth, J., Vestergaard, M., Sorensen, A. N., & Grundahl, F. 1995, *ApJ*, 452, L17
- Hua, C. T. 1988, *A&A*, 199, 105
- Jahnke, K. 2002, Ph.D. thesis, Univ. Hamburg, <http://www.sub.uni-hamburg.de/disse/726/dissertation.pdf>
- Jahnke, K., Wisotzki, L., Sánchez, S., Christensen, L., Becker, T., Kelz, A., & Roth, M. 2004, *Astron. Nachr.*, 325, 128
- Jedrzejewski, R. I. 1987, *MNRAS*, 226, 747
- Mediavilla, E., et al. 1998, *ApJ*, 503, L27
- Moles, M., del Olmo, A., Masegosa, J., & Perea, J. D. 1988, *A&A*, 197, 1
- Osterbrock, D. E. 1989, *Astrophysics of Gaseous Nebulae and Active Galactic Nuclei* (Mill Valley: University Science Books)
- Peng, C. Y., Ho, L. C., Impey, C. D., & Rix, H. 2002, *AJ*, 124, 266
- Pérez-Fournon, I., Colina, L., Biermann, P., & Marcaide, J. M. 1986, in *IAU Symp. 119, Quasars*, ed. G. Swarup & V. K. Kapahi (Dordrecht: Reidel), 127
- Sánchez, S. 2004, *Astron. Nachr.*, 325, 167
- Sánchez, S. F., et al. 2004, *ApJ*, in press (astro-ph/0403645)
- Solórzano-Iñarrea, C., & Tadhunter, C. N. 2003, *MNRAS*, 340, 705
- Soubeyran, A., Wlerick, G., Bijaoui, A., Lelievre, G., Bouchet, P., Horville, D., Renard, L., & Servan, B. 1989, *A&A*, 222, 27
- Veilleux, S., & Osterbrock, D. E. 1987, *ApJS*, 63, 295
- Villar-Martín, M., Tadhunter, C., Morganti, R., Axon, D., & Koekemoer, A. 1999, *MNRAS*, 307, 24
- Walker, R. C. 1997, *ApJ*, 488, 675
- Walker, R. C., Benson, J. M., & Unwin, S. C. 1987, *ApJ*, 316, 546
- Walker, R. C., Walker, M. A., & Benson, J. M. 1988, *ApJ*, 335, 668
- Wisotzki, L., Becker, T., Christensen, L., Helms, A., Jahnke, K., Kelz, A., Roth, M. M., & Sanchez, S. F. 2003, *A&A*, 408, 455
- Wlerick, G., Cayatte, V., Michet, D., & Bouchet, P. 1981, *A&A*, 102, L17